-RESEARCH PAPER-

International Journal of Mining and Geo-Engineering

IJMGE

IJMGE 57-1 (2023) 89-99

DOI: 10.22059/IJMGE.2023.351885.595004

3D inversion of magnetic data using Lanczos bidiagonalization and unstructured element

Khatereh Danaei [a] , Ali Moradzadeh [a, *], Gholam-Hossain Norouzi [a] and Maysam Abedi [a]

[a] *School of Mining Engineering, College of Engineering, University of Tehran, Tehran, Iran.*

Article History:
Received: 30 November 2022.
Revised: 01 January 2023.
Accepted: 06 January 2023..

ABSTRACT

This work presents an algorithm to construct a 3D magnetic susceptibility property from magnetic geophysical data. Physical model discretization has substantial impact on accurate inverse modeling of the sought sources in potential field geophysics, where structural meshing suffers from edge preserving of complex-shaped geological sources. In potential field geophysics, a finite-element (FE) methodology is usually employed to discretize the desired physical model domain through an unstructured mesh. The forward operator is calculated through a Gauss-Legendre quadrature technique rather than an analytic equation. To stabilize mathematical procedure of inverse modeling and cope with the intrinsic non-uniqueness arising from magnetometry data modeling, regularization is often implemented by utilizing a norm-based Tikhonov cost function. A so-called fast technique, "Lanczos Bidiagonalization (LB) algorithm", can be utilized to solve the central system of equations derived from optimizing the function, where it decreases the execution time of the inverse problem by replacing the forward matrix with a lower dimension one. In addition, to obtain best regularization parameter, a weighted generalized cross-validation (WGCV) curve is plotted, that makes a balance between misfit norm and model norm introduced in the cost function. In order to tackle the normal propensity of physical structures to focus at the shallow depth, an expression of depth weighting is used. This procedure is applied to a synthetic scenario presenting a complex-shaped geometry along with a real set of magnetic data in central part of Iran. So the capability of the proposed algorithm for inversion indicates the accuracy of the inversion algorithm. Additionally, the modeling results pertaining to a field case study are in good agreement with the drilling data.

Keywords: *Unstructured meshing, Magnetic data inversion, LB algorithm, WGCV, Iron deposit..*

1. Introduction

The magnetic technique has wide usage including hydrocarbon and mineral prospecting, tectonic structure identification, along with environmental and engineering investigations. For imaging physical properties of a target, inversion of geophysics data has a significant role [1], wherein the physical features of subsurface are obtained linearly or non-linearly from geophysical data [2]. To understand the physics of the source, inversion utilizes a set of mathematical procedures to estimate sought physical model [3]. Some prior information about the searched model, and many geological/geophysical data are often required to control the intrinsic non-uniqueness arising from geophysical data inversion [4, 5]. An inverse problem is generally divided into two parts: element-based physical property modeling, and simple-shaped parametric modeling of sought sources [6].

From geophysical point of view, the main application of parametric methods on geophysics data is in simple-body geometries that, mainly through interaction of computers and humans, the best parameters of shape are obtained with regards to the rough body [7, 8]. Especially when the rough geometry is close to the simple form, geophysical data will give out good results. It is worth pointing out that less time needed to apply this type of process. In the case of targets with complicated forms, when applying the parametric inversion, no sufficient information would be available. Therefore, a divided subsurface is necessary to obtain physical properties. As we know, iterative method is hard and takes a lot of time but in the case of complex-shaped geometries is very useful. Note that the rough body in both approaches assume there is physical contrast in the geological setting [9].

To tackle non-unique response, the cell-based minimum-structure approach is used. However, this inversion approach, that includes many unknown factors, requires a lot of time [10]. Note that imaging the complicated geology structures is an important process in geophysics to obtain susceptibility and density properties. Li and Oldenburg (1998, 2003) used some techniques for the inversion, such as a new regularization method, to obtain correctly the geometry of a sought body by minimizing an objective function, including a model stabilizer and a misfit. Also, optimizing the speed of calculations is an attractive idea in the field of geophysics. In all methodologies, addition of drilling information and geological observation has significant impact on correct recovering of the sough target [12]. An L_P-norm cost function is regularized to solve the linear model in the geophysical method [13], where the rate of robustness and convergence increases by using a weighted parameter in iterative inversion procedure [14].

Geophysicists are attentive in the simpler gravity and magnetic forward modeling and utilizing the structural mesh subdivisions. Although in complicated topography and geology, the quadrature element is suitable. So, to recreate any rough body and topography and make a suitable valuation of geology forms, unstructured meshes with less elements are used in the current research work in this field [15, 16]. Triangular/tetrahedron meshing through the Delaunay rule is a new technique and is a popular approach for physical model discretization [17, 18]. So, to get a proper body with complex geometry and rough

---

* Corresponding author: *E-mail address:*: a_moradzadeh@ut.ac.ir (A.i Moradzadeh).

topography, non-structured grid is extensively used [17, 19, 20].

To integrate isoperimetric elements in this research, Gauss-Legendre quadrature is used. Also, other methods of finite element (FE) such as structured (Cai and Wang., 2005) and unstructured mesh were applied [21, 22]. Note that Gauss-Legendre quadrature in irregular elements has been shown useful for 2D magnetotelluric (MT) and 2.5D controlled-source electromagnetic (CSEM) modeling in complex structures and topography. In another work of Delaunay tetrahedral elements, irregular mesh was used on the gravity data [23]. They pointed out, the finite element method is more correct even though it requires more computational power. Also, non-rectangular mesh, in body-growth technique was used by Kim et al (2014) for inversion of magnetic data [24]. Moreover, Gross et al (2015) used the finite element procedure in inversion of geophysical data on parallel systems [25]. Roussel et al (2015) computed the gravity gradient method and compared numerical and analytical systems for simple shapes. Then Gauss-Legendre quadrature with ellipsoidal cells were used by them to evaluate the gravity anomaly [26]. In the other work, in inverse and forward problem, for answering partial differential expressions, the FE method was used by Schaa et al (2016) with constraint border settings [27]. Li et al (2018) used a finite element time-domain (FETD) electromagnetic forward method for a complicated body transmitting loop, where an irregular tetrahedral grid was used in the total-field algorithm [28]. Furthermore, Uwiduhaye et al (2019) estimated the density property of gravity anomaly by hexahedral meshes with Gauss-Legendre integration in a geothermal survey [29]. Finally Codd et al (2021) proposed a fast inversion process for gravity or magnetic data, based on a finite element technique discretization by unstructured tetrahedral meshes [30].

In addition, a quick procedure that is called the least-squares QR (LSQR) technique is used to decrease the calculation time and it is like the core of the LSQR method (Lanczos bidiagonalization "LB"). This solver is better in respect with direct method as conjugate gradient (CG) systems [31, 32]. So, in order to save the basic vectors, the LB method is suitable because it uses less memory and smaller dimensions of the matrix in the computation. An important difficulty in geophysics modeling is the ill-posed problem of the equations to be solved. That causes non-uniqueness outcomes. So, in order to stabilize the obtained response and minimize the objective function, Tikhonov and Arsenin (1977) used regularization via the objective function including a model norm and a misfit. To reach this goal, a suitable regularization parameter that causes an ideal balance between model norm and the misfit should be chosen. As the resulting model of the Tikhonov regularization is usually smooth, a depth weighting factor in the objective inversion function is inserted to obtain the best result in the depth [33].

As mentioned, many types of inversion techniques are used by researchers to obtain precious outcomes. In order to solve the inverse models, the subsurface is divided to regular and irregular elements in various 3D systems. The review of the aforementioned published papers indicates that, none of them has described obviously how the equations of the irregular element is set together in 3D magnetic data inversion. Thus, to model the magnetic data accurately using unstructured FE elements, an inversion system is presented in this paper. Mesh generation is planned with TetGen package in MATLAB. Also, the LB technique used to accelerate the running process of the inversion.

The following parts of this paper are presented as bellow. Part 2 explains the principle of FE on forward modeling and application of the LSQR technique in inversion process. Part 3 discusses the efficacy of the proposed 3D magnetic inversion method by applying on synthetic model. In Part 4, geophysical survey, geological setting and inversion of real magnetic data of Yazd area, are explained as a case study. Finally, the study finishes with an outcomes part.

2. Material and methods

The proposed technique is used to perform with unknown susceptibility in any irregular subsurface hexahedral meshes. So, the inversion procedure is explained in the following part. In inversion process, the physical properties of the subsurface model are related to the observed magnetic data by a linear set of equations [34]. In the next two sections, the way of expressing the forward modeling with the FE method for an irregular mesh and also the process of solving the system of linear equations with the LSQR method are concisely described.

2.1. Forward modeling

For defining a complex-shaped topography and geological model, structured mesh discretization is an obstacle. Therefore, for attacking these matters the irregular mesh is a remedy. The exact outcomes on the rough topographical data are possible to attain via one of the aspects of the mesh. There are two main features in using the unstructured mesh: (1) through reducing the number of model parameters, the size of inverse problem decreases; and (2) the capability to correctly display any rough surfaces. Here, the subsurface model is divided to irregular meshes with several magnetic susceptibility. To calculate the physical property, an analytical solution could be obtained in a special cell with a unique property [18].

In this study, in regard to irregular division in the forward process, it is supposed that physical properties in each cell is homogenous. The subsurface discretized to cells and the magnetic anomaly of individual mesh are calculated as follow, then can be added to compute the data at each point, i, as [2]:

$$\mathrm{d_i} = \sum_{j=1}^{m} \mathrm{A_{ij}} k_j\,, \quad \mathrm{i} = 1, \dots, \mathrm{n} \tag{1}$$

where $\mathrm{A_{ij}}$ is the kernel that relates the magnetism at the observation i to the cell j , 'k' stands for the subsurface meshes with magnetic susceptibility contrast (κ_j), n represents the number of observation data and '$\mathrm{d_i}$' is the magnetic anomaly. Figure 1 shows the procedure of the subsurface area discretization to the irregular hexahedron cells and converting four of them to a tetrahedral mesh by TetGen package.

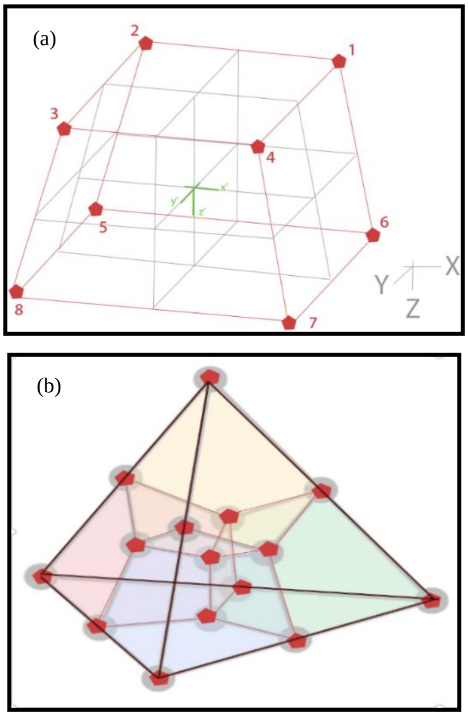

Figure 1. (a) The local coordinate axis (x',y',z') of an irregular hexahedron, and (b) a tetrahedral shape created by 4 hexahedral elements.

It is expected that the noise, e_i related with each observed data has a Gaussian distribution and is uncorrelated with each other. So, the observed data is shown by matrix as:

$$d_{obs} = \mathrm{d_i} + e_i\,, \tag{2}$$

where $e_i \in \mathrm{R^n}$ is the noise in the $\mathrm{i^{th}}$ observation data. The $\mathrm{A_{ij}}$ is the kernel matrix, as [24],

$$\mathrm{A_{ij}} = \frac{k}{4\,\pi} \int_{\mathrm{V_j}} \left[\frac{(2\mathrm{S_x}-\mathrm{S_y}-\mathrm{S_z})\mathrm{X}^2+(2\mathrm{S_y}-\mathrm{S_x}-\mathrm{S_z})\mathrm{Y}^2+(2\mathrm{S_z}-\mathrm{S_y}-\mathrm{S_x})\mathrm{Z}^2+3(\mathrm{S_{xy}XY}+\mathrm{S_{yz}YZ}+\mathrm{S_{zx}ZX})}{(\mathrm{X}^2+\mathrm{Y}^2+\mathrm{Z}^2)^{5/2}}\right] \mathrm{dV} \qquad (3)$$

Here X = x–x_i, Y = y– y_i, Z = z– z_i in which x_i, y_i, z_i and x, y, z respectively are coordinate location of the observation and the vertices of cells, also v_j is the volume of j^th^ mesh. The coefficients S_x, S_y, S_z, S_{xy}, S_{yz} and S_{zx} are given below respectively:

$$\mathrm{S_x = K_xH_x}\,, \qquad \mathrm{S_y = K_yH_y}\,, \qquad \mathrm{S_z = K_zH_z}$$
$$\mathrm{S_{xy} = K_xH_y + K_yH_x}\,,\ \mathrm{S_{yz} = K_yH_z + K_zH_y}\,,\ \mathrm{S_{zx} = K_zH_x + K_xH_z}$$
$$\mathrm{H_x = \cos D_m \cos I_m}\,,\ \mathrm{H_y = \sin D_m \cos I_m}\,,\ \mathrm{H_z = \sin I_m}$$
$$\mathrm{K_x = \cos D_f \cos I_f}\,, \qquad \mathrm{K_y = \sin D_f \cos I_f}\,, \quad \mathrm{K_z = \sin I_f}$$

The integral in Eq. (3) is calculated by a Gauss-Legendre quadrature method. Because of the logarithm and arctangent expressions in forward modeling particularly on the non-rectangular meshes, forward modeling is taken more time in analytical procedures. It is important to note that the Gaussian–Legendre procedure is more accurate than other numerical methods such as Romberg or trapezoidal integration. Thus, we used the following 3D Gauss–Legendre integration to estimate Eq. (3) like the procedure of Kim et al. (2009),

$$\int_{-1}^{1}\int_{-1}^{1}\int_{-1}^{1} f(x',y',z')dx'dy'dz' = \sum_{o=1}^{b} w_o \sum_{a=1}^{b} w_a \sum_{t=1}^{b} w_t\, f(x'_o, y'_a, z'_t), \qquad (4)$$

where 'b' is the number of points in Eq. (3) and f is the integrand, which the 'f' calculates in the local coordinates; x'_o, y'_a, z'_t are the local coordinates system. Furthermore, in the global coordinate structure, w_o, w_a, w_t are the weight factors of the o^th^, a^th^, t^th^ subdivision on the X, Y, Z axis. Now, for example, for b = 4, the w_o weight constants of Gauss–Legendre value and the values of coordinates x'_o are given in Table 1.

Table 1: The weight coefficients and coordinates of Gauss–Legendre basis for b=4 (Kim et al., 2009).

b	x'_o	$\mathrm{w_o}$
4	0.8611363115940533	0.347854845137454
	-0.8611363115940533	0.347854845137454
	0.339981043584856	0.652145154862525
	-0. 339981043584856	0.652145154862525

Therefore, for the irregular mesh, the kernel is [24]:

$$\mathrm{A_{ij}} = \frac{k}{4\,\pi} \sum_{\mathrm{p}=1}^{\mathrm{b}} \mathrm{w_p} \sum_{\mathrm{q}=1}^{\mathrm{b}} \mathrm{w_q} \sum_{\mathrm{r}=1}^{\mathrm{b}} \mathrm{w_r}\, \mathrm{D_{pqr}} \qquad (5)$$

where the term $\mathrm{D_{pqr}}$ is:

$$\mathrm{D_{pqr}} = \frac{(2\mathrm{S_x}-\mathrm{S_y}-\mathrm{S_z})\mathrm{X}^2+(2\mathrm{S_y}-\mathrm{S_x}-\mathrm{S_z})\mathrm{Y}^2+(2\mathrm{S_z}-\mathrm{S_y}-\mathrm{S_x})\mathrm{Z}^2+3(\mathrm{S_{xy}XY}+\mathrm{S_{yz}YZ}+\mathrm{S_{zx}ZX})}{(\mathrm{X}^2+\mathrm{Y}^2+\mathrm{Z}^2)^{5/2}} \mathrm{V_{pqr}} \qquad (6)$$

and $\mathrm{V_{pqr}}$ is the Jacobian matrix that is explained by Eq. (9). Also, x, y, z could be put at expression of the local coordinates system (x'_o, y'_a, z'_t), as

$$x = \sum_{c=1}^{8} J_c x_c\,, \quad y = \sum_{c=1}^{8} J_c y_c\,, \quad z = \sum_{c=1}^{8} J_c z_c \qquad (7)$$

J_c is a shape function that is explained in Eq. (8) and local coordinates of vertices x'_c, y'_c, z'_c (c = 1, ⋯, 8) are shown in Table 2 [35]:

$$J_c(x',y',z') = \frac{1}{8}(1 + x'x'_c)(1 + y'y'_c)(1 + z'z'_c), \quad c = 1, \ldots, 8 \qquad (8)$$

The determinant of the Jacobian matrix, explains $\mathrm{V_{pqr}}$ in Eq. (6) so:

$$V(x',y',z') = \det \begin{pmatrix} \frac{\partial x}{\partial x'} & \frac{\partial y}{\partial x'} & \frac{\partial z}{\partial x'} \\ \frac{\partial x}{\partial y'} & \frac{\partial y}{\partial y'} & \frac{\partial z}{\partial y'} \\ \frac{\partial x}{\partial z'} & \frac{\partial y}{\partial z'} & \frac{\partial z}{\partial z'} \end{pmatrix} \qquad (9)$$

So, by differentiating Eq. (7), the components of matrix (9) are:

$$\frac{\partial x}{\partial x'} = \sum_{c=1}^{8} \frac{\partial J_c}{\partial x'} x_c, \ \frac{\partial y}{\partial x'} = \sum_{c=1}^{8} \frac{\partial J_c}{\partial x'} y_c, \ \frac{\partial z}{\partial x'} = \sum_{c=1}^{8} \frac{\partial J_c}{\partial x'} z_c\,, \ \frac{\partial x}{\partial y'} = \sum_{c=1}^{8} \frac{\partial J_c}{\partial y'} x_c,$$
$$\frac{\partial y}{\partial y'} = \sum_{c=1}^{8} \frac{\partial J_c}{\partial y'} y_c\,, \frac{\partial Z}{\partial y'} = \sum_{c=1}^{8} \frac{\partial J_c}{\partial y'} z_c, \ ,\frac{\partial x}{\partial z'} = \sum_{c=1}^{8} \frac{\partial J_c}{\partial z'} x_c, \ \frac{\partial y}{\partial z'} = \sum_{c=1}^{8} \frac{\partial J_c}{\partial z'} y_c,$$
$$\frac{\partial Z}{\partial z'} = \sum_{c=1}^{8} \frac{\partial J_c}{\partial z'} z_c \qquad (10)$$

Table 2: In the local coordinates systems, Apices of the hexahedral cell is displayed in Fig. 1a (Kim et al. 2009).

L	1	2	3	4	5	6	7	8
x'_c	-1	1	-1	1	-1	1	-1	1
y'_c	-1	-1	1	1	-1	-1	1	1
z'_c	-1	-1	-1	-1	1	1	1	1

Thus, by differentiating Eq. (8), the derivatives of shape functions are obtained [35]:

$$\frac{\partial J_c}{\partial x'} = \frac{x'_c}{8}(1 + y'^{y'_c})(1 + z'^{z'_c}), \ \frac{\partial J_c}{\partial y'} = \frac{y'_c}{8}(1 + x'^{x'_c})(1 + z'^{z'_c})\,, \ \frac{\partial J_c}{\partial z'} = \frac{z'_c}{8}(1 + x'x'_c)(1 + y'y'_c) \qquad (11)$$

$$P(x',y',z') = \left(\frac{\partial x}{\partial x'} \times \frac{\partial y}{\partial y'} \times \frac{\partial z}{\partial z'}\right) + \left(\frac{\partial x}{\partial y'} \times \frac{\partial y}{\partial z'} \times \frac{\partial z}{\partial x'}\right) + \left(\frac{\partial x}{\partial z'} \times \frac{\partial y}{\partial x'} \times \frac{\partial z}{\partial y'}\right) - \left(\frac{\partial z}{\partial x'} \times \frac{\partial y}{\partial y'} \times \frac{\partial x}{\partial z'}\right) - \left(\frac{\partial z}{\partial y'} \times \frac{\partial y}{\partial z'} \times \frac{\partial x}{\partial x'}\right) - \left(\frac{\partial z}{\partial z'} \times \frac{\partial y}{\partial x'} \times \frac{\partial x}{\partial y'}\right)$$

2.2. The LSQR algorithm for inversion

The valuation of the magnetic susceptibility is the goal of inversion for the subsurface structure. The outcome of inversion is usually non-unique, unstable and ill-posed. So, to get the best answers, the Tikhonov cost function must be minimized [1]:

$$\delta(k) = \delta_d(k) + \alpha\, \delta_m(\mathrm{k}) \qquad (12)$$

Here α is a regularization term that balances model misfit function, $\delta_d(k)$, and model norm $,\delta_m(k),$ during minimizing of the $\delta(k)$, objective function for inversion of the observed data. This equation can be written as:

$$\delta(k) = \left\|w_f(Ak - d)\right\|_2^2 + \alpha\|w_z(k)\|_2^2 \qquad (13)$$

with; $w_z = (z + z_0)^{-3/2}$

Here w_z is a depth weighting matrix $(z + z_0)^{-3/2}$ in which z_0 is a small constant for suppressing singularity, z is the mean depth of each element and the power value is 3/2 since the effect of a cubic-form declines by inverse distance with a structural index 3. This depth weighting factor causes an accurate inversion result as it sets a larger importance on the deeper section. The data weighting matrix is also given as:

$$w_f = diag\,(1/\tau_1\,, 1/\tau_{\mathrm{R}}\,, \ldots, 1/\tau_n)\,, R = 1, \ldots, n \qquad (14)$$

Here τ_R is the noise standard deviation in the R^th^ data.

Next, like Pilkington (1997) [36] and Meng et al. (2017) [37], we can write it as below;

$$\begin{bmatrix} w_f A \\ \alpha^{\frac{1}{2}} w_z \end{bmatrix}(k) = \begin{bmatrix} w_f d \\ 0 \end{bmatrix} \qquad (15)$$

Or equivalently expressing a vector β and matrix ε

$$\varepsilon k = \beta \qquad (16)$$

For minimizing the linear term (like the above matrix) iterative system uses the LSQR process (this method was described in many articles mentioned in the introduction section, so it is avoided any extra explanation about it). The misfit of the model response with the observed data is then assessed by the RMS error [38-40].

For solving the ill-posed problem and a large linear expression, the LSQR technique (or LB solver) uses an iterative procedure. This method is faster than the conjugate gradient (CG) technique for solving Tikhonov regularization problems. In this method the matrix dimension of the subsurface area is small enough and it causes the LSQR procedure consumes less time and computer RAM in contrast to the direct procedures [41].

In the following part, the optimum regularization amount α (regularization parameter) and I (steps of the LB solver) is obtained by the weighted-GCV (WGCV) with presumption w=0.5 in synthetic and real case which is an appropriate technique [42]. Note that the ideal regularized answer is matched to the regional minimum of the WGCV curvature that the w constant is stable in the range (0,1). Now, at the end of this part, the flowchart of the proposed modeling algorithm is drawn to clarify the work steps (Figure 2).

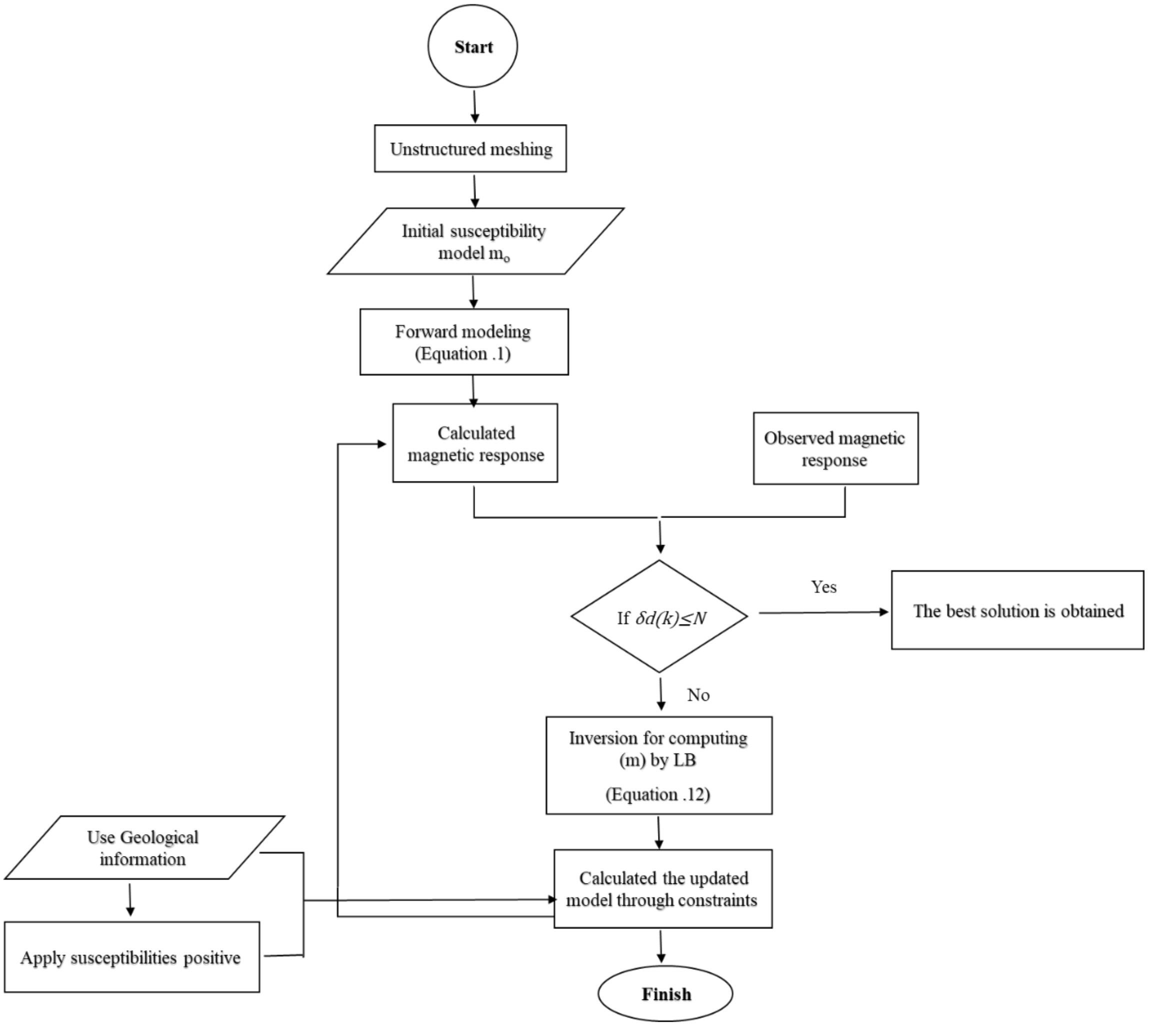

Figure 2. Workflow for inversion the proposed algorithm on magnetic data.

3. Synthetic data inversion

To assess the efficiency of the suggested inversion algorithm, it was first applied on a synthetic magnetic data. This model contains a rough shape under the surface that is divided into 38568 irregular hexahedral meshes as displayed in Figure 3a and in Figures 3b, 3c and 3d, with cross-section in X=100 m, Y=100 m and Z= -100 m. The specification of the model includes the magnetic susceptibility of the target, the Earth's magnetic field intensity (B), angles of declination (D°), inclination (I°) and depth of the body which are assumed to be equal to 0.05 SI, 47500 nT, 2°, 50° and 50 meters respectively.

The magnetic response of the body is displayed in Figure 4a, with a 5% contaminated Gaussian noise. The whole number of data is 121 with spacing of 20 m on a 200 m × 200 m grid displayed in Figure 4b.

To obtain the magnetic susceptibility model and evaluate the effect of low dimension forward kernel in reproducing exact rough model, some *l* step is performed by the LSQR technique. In Figures 5a to 5c, the cross-section at X = 100 m and Y = 100 m and the results of the inversion are presented (the outcome is displayed with green and rough model exposed with dark blue which fits together wonderfully but the proposed process is a slightly bigger response). Here a kernel matrix with less dimensionality is replaced with the forward matrix $G_{121\times38568}$ (121 and 38568, are respectively the numbers of data and the meshes). Approximately all obtained answers were appropriate and very similar in some steps. Thus, it is not necessary to increase the number of steps because the outcomes are not different outside as l=100 that the running time is 0.4643 s. In Figure 6, the running time on a processer with a 64-bit operation system, 32-GB RAM, 2.4 GHz CPU, and Core i7-8750H for *l* step was shown. It is seen that increasing *l* causes the running time to be higher in obtaining the magnetic susceptibility model.

To obtain reasonable results, a suitable regularization factor is necessary. We ran 3D inversion with different value of w from 0 to 1 and found that w =0.5 produces the best value of the regularization parameter $\alpha = 4\times10^9$ when the amount of the WGCV is minimized. The RMS error among the predicted and the synthetic magnetic data was found around 0. 7% which hints the accuracy of the results.

4. Real data

In Iran, several kinds of Iron reserves are formed. The main iron targets were made in Cenozoic and the Neoproterozoic-early Cambrian [43, 44]. More than 4 billion tons of iron deposits in Iran include placer deposits, iron oxide copper gold (IOCG), magmatic ores, skarn, magnetite-apatite, Kiruna-type and volcano-sedimentary reserves. The main structural regions of iron host resources include Zagros, Bafq-Posht-e-Badam back arc region, and Sanandaj-Sirjan metamorphic region (Fig. 7). Moreover, Urumieh-Dothtar and Alborz area have some occurrence of iron resources. In Iran, iron mineralization is in three eras [44]: (1) Paleozoicearly Mesozoic (volcano-sedimentary), (2) Cenozoic (skarn, placer, magmatic, IOCG and Kiruna-kind), and (3) the Neoproterozoic-early Cambrian (Kiruna-type and volcano-sedimentary).

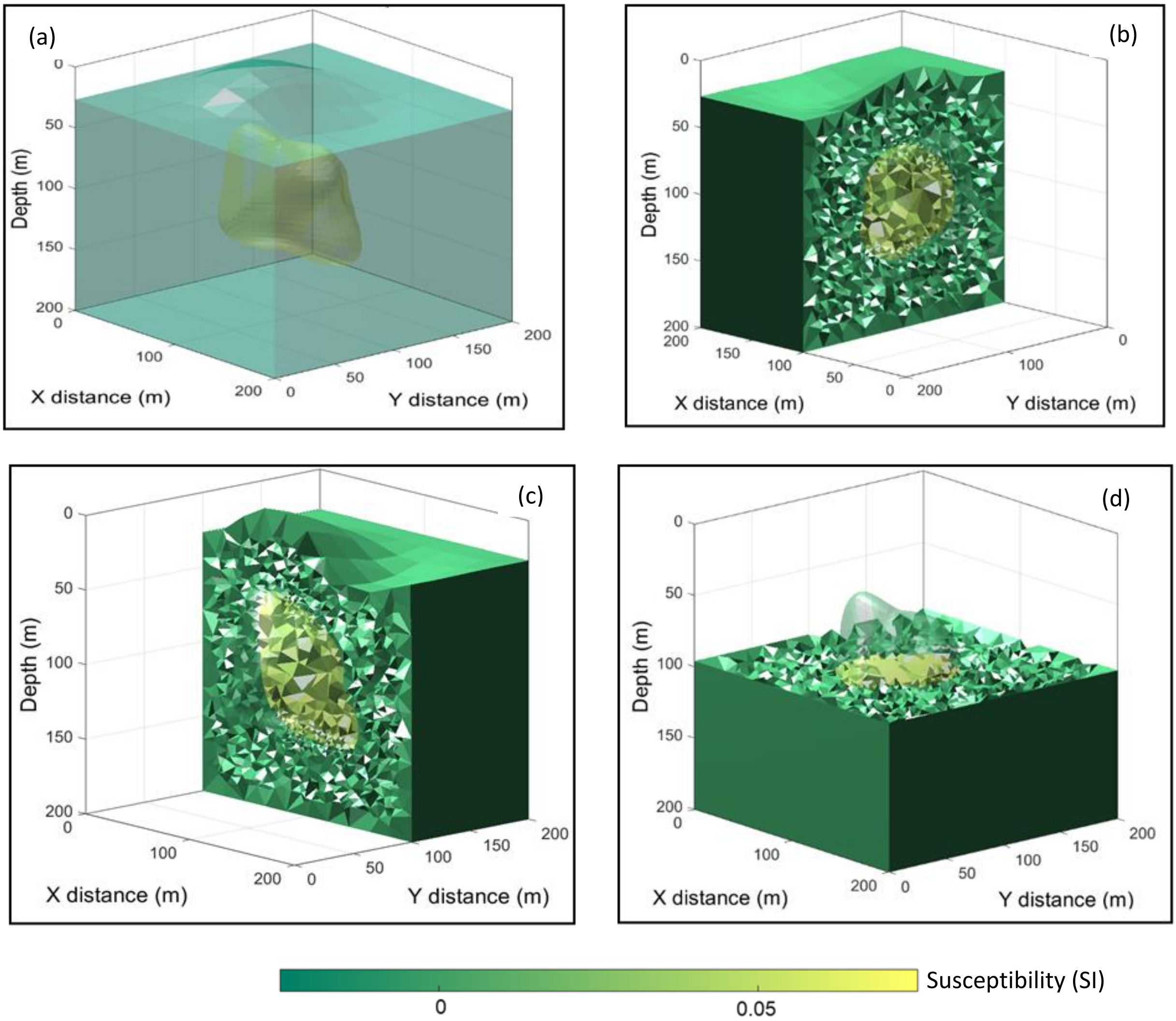

Figure 3. (a) A three-dimensional synthetic model, (b) the model's cross-section in X = 100m, (c) the model's cross-section in Y = 100m, and (d) the model's cross-section in Z = −100 m.

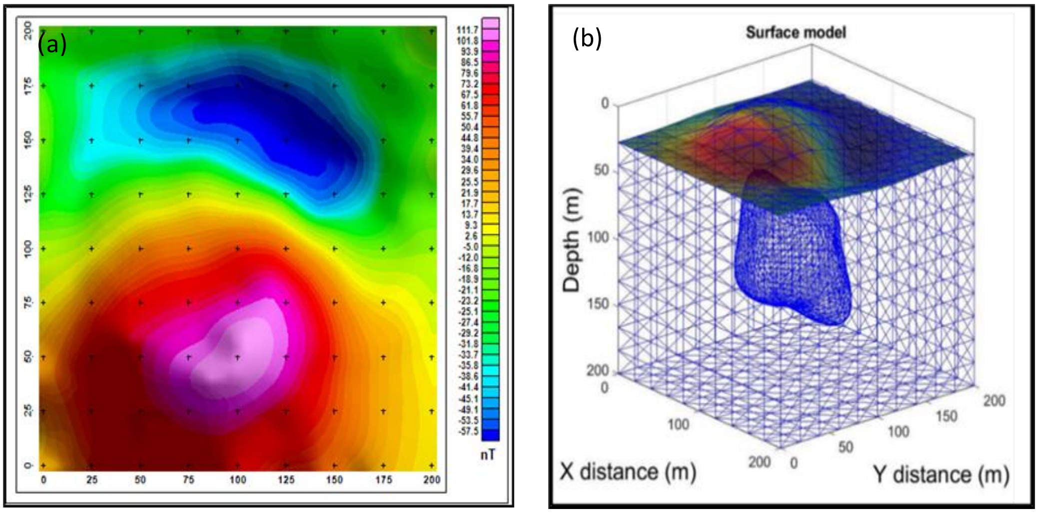

Figure 4. (a) The synthetic model's response (with 5% Gaussian noise), and (b) a 3D synthetic model with residual magnetic anomaly and ground topography.

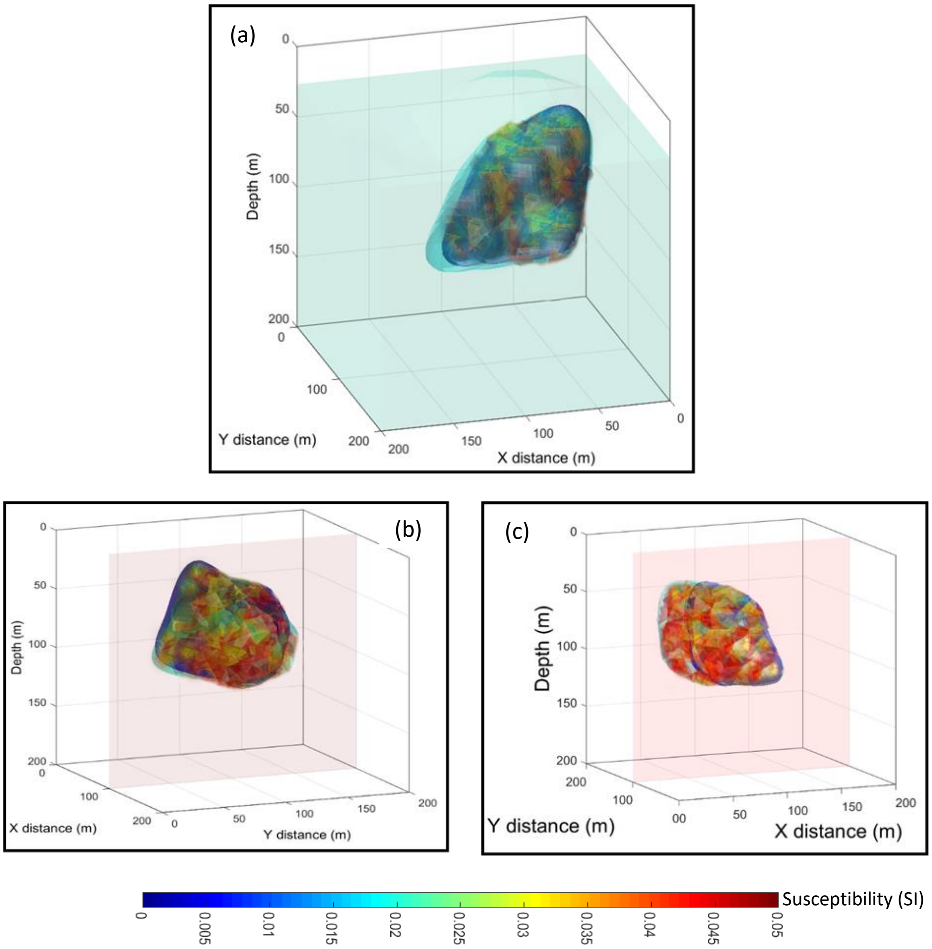

Figure 5. (a) Perspective view of inversion result with cut-off (0.35-0.7 SI in susceptibility) and l=100, (b) the model's cross-section in X = 100m, and (c) the model's cross-section in Y = 100 m.

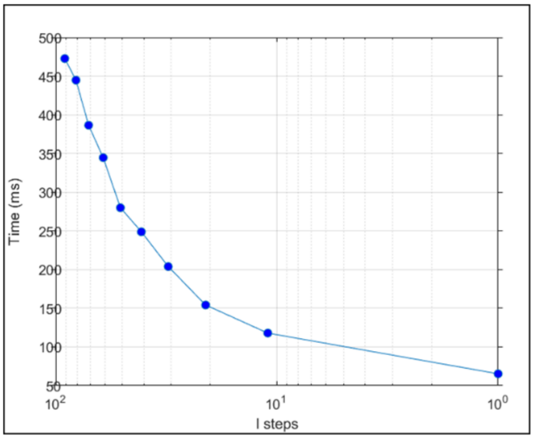

Figure 6. Time of inversion process for several l steps.

The area that its real ground magnetic data is used in this study locates in the Kafeh-E-Taghestan region with latitude and longitude of 31^0 36' and 53^0 39' respectively. It is in 25 kilometers SW of Shavaz region and 170 km from Yazd province. In the next sub-sections geology of the area and data modeling is explained.

4.1. Geological setting

The area has high potential due to metalliferous incidences, which are magnetite and hematite [45]. The mineralization of this area is shaped along the Nain-Dehshir-Baft fault where a collection of pelagic limestones (upper Cretaceous defined by microscopic fossils), radiolarite and ultrabasic rocks (gabbro pegmatoid and serpentinite) are present along the Dehshir-Baft fault. It can be seen on the geological map that the study area has the outcrops of andesite and diabase and more coverage of Kerman conglomerate and alluvial (Fig. 7). Also, classifications of andesite, shale and dolomitic can be seen in the nearby region. On the edge of andesitic rocks, tuff and small amounts of magnetite and hematite can be seen [46].

The granodiorite rocks and Shirkuh granite (acidic composites and biotite granodiorites) in the east in this region were for lower Cretaceous. Limestone with gabbro-diorite, red marls and conglomerates are the lithology of the Sangestan formation. Also, the Shirkuh granite is under the Sangestan formation and belongs to early Cretaceous [47]. The unit overlying the Lower Cretaceous has dolomitic-limestone composition in the Taft formation.

4.2. Inversion of real data

The magnetic data was acquired using a grid of 550× 650 m with spacing of 20 and 40 m along the x axis, and 10 and 20m along the y axis. Figure 8a shows two anomalous regions maybe related to iron mineralization on the residual magnetic map with 1641 observation points. Figure 9 shows the study area that is divided to irregular elements with topography relief. Also the optimum value 10^6 for α produced the minimum amount of the WGCV. Considering the presence alluvial sediments as background geological unit, a constraint was applied on inversion of geophysical data to keep the mesh susceptibilities positive. The results of 3D inversion are given as some magnetic susceptibility cross-section at X = 727500 m, 727600 m, 727700 m and Y = 3507100 m, 3507200 m, 3507300 m and Z = 50, 150, 250 m

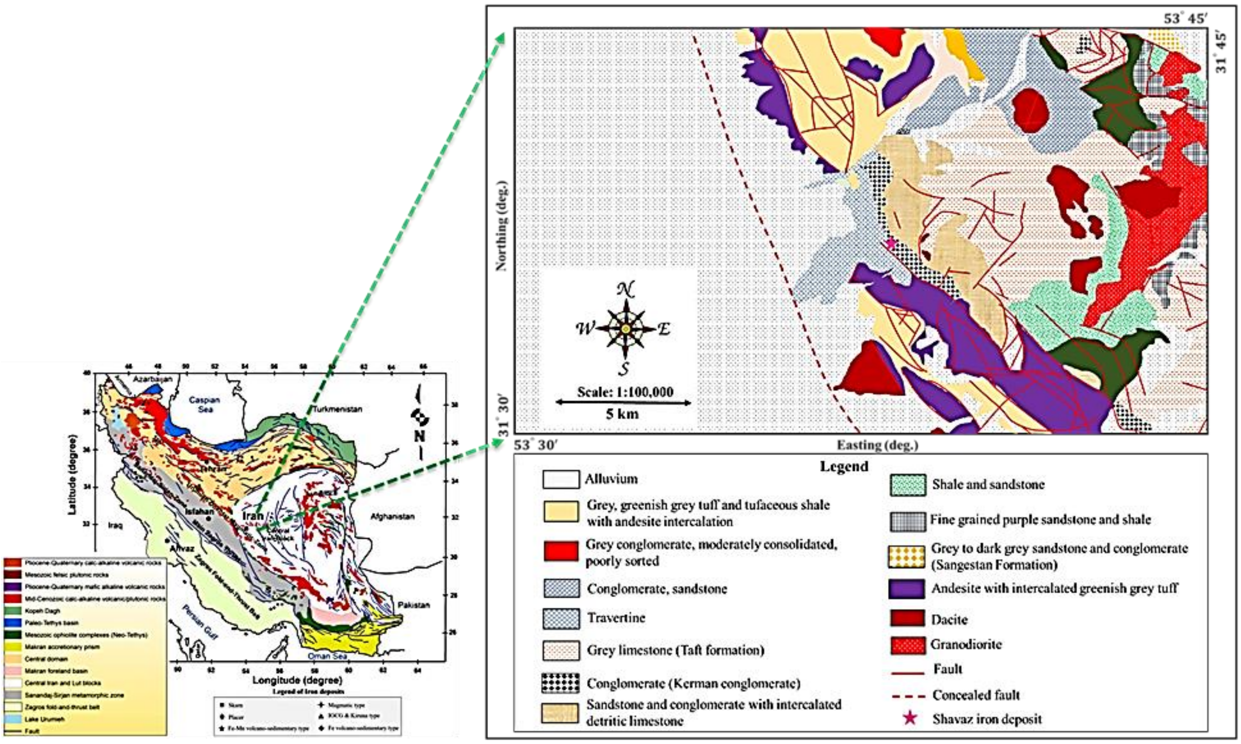

Figure 7. A schematic structural map of Iran including thrusts and strike-slip faults. The study area has shown with a rectangle on it. A simplified geological map of the Shavaz area was provided on the right side of this Figure. [48].

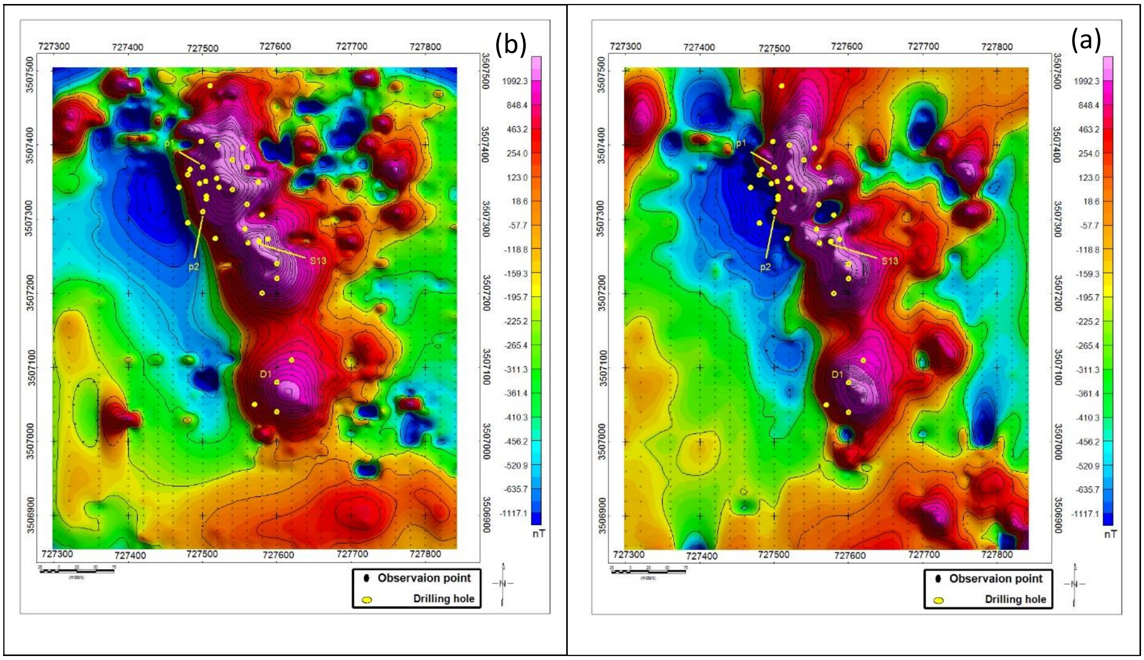

Figure 8. (a) The map of residual measured magnetic data, and (b) the map of predicted (model response) magnetic data..

respectively in Figures 10a-10g. Furthermore, Figures 11a-b display the recovered model with cut-off values of 0.45-0.8 and 0.1-0.95 SI magnetic susceptibility at the *l*-steps of 100 of inversion process. It illustrates that the recovered model has the highest volume of response over an area with 400 meter length in the center of model. The predicted magnetic data is shown in Figure 8b.

The difference between the predicted and the observation magnetic response is shown by the RMS error which was found around 4.9% on real data. Also the regression coefficient is 0.90 that this amount of error indicates the accuracy of the inversion results for real data. To get this inversion results, the size of elements was decreased on shallow depth and increased with depth. Additionally, the model space at the borders was increased to remove the border error. Moreover, to remove any regional effect which may exist, the padding cells around boundaries were added.

Figure 11 depicts the results of 3D inversion of magnetic data as 2D section at X= 727600 m with some drilled boreholes along it. This cross section displays two different regions of high magnetic susceptibility values along the depth of 60 to 250m which may indicate the iron ore mineralization. The running time of inversion was around 17.45 seconds

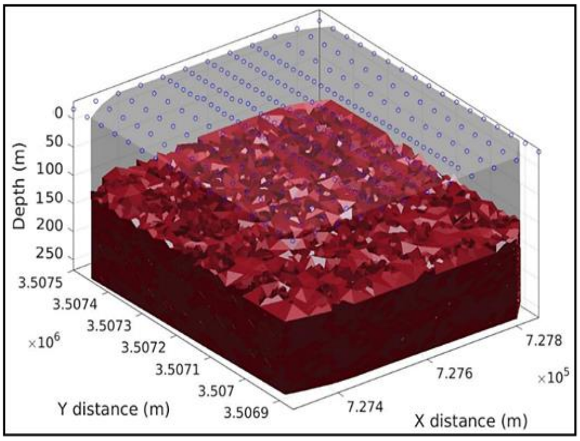

Figure 9. Division of the study region with a mild topography using the irregular elements..

based on the proposed inversion routine for the obtained model. The computer configuration was the same as mentioned for inversion of the synthetic data.

Figures 7a and 7b, show 34 boreholes (yellow points), out of which four of them (P2, S13, P6 and D1 on Figure 12) are selected to evaluate the outcomes of 3D inversion. Figure 13 shows depth of hole, results of inverse modelling (as magnetic susceptibility log), the total Fe weight percent of core drilling and their geological logs on each these 4 core drilled. As can be seen in the figures, in borehole No. P6, the most enrichment of ore mineralization was occurred at the depth intervals of 34-46 m (50.01% is grade of Fe) that has notable relationship with the inversion result that shows the magnetic susceptibility of about 0.8 in this depth interval. The similar matching settings are iterated at other boreholes. Enrichment in mineralization of iron ore in these 4 boreholes along with their depth intervals are given in Table 3.

It is seen that the obtained results of 3D inversion are in good agreement with those boreholes. This is another reason for proficiency of the proposed 3D inversion algorithm.

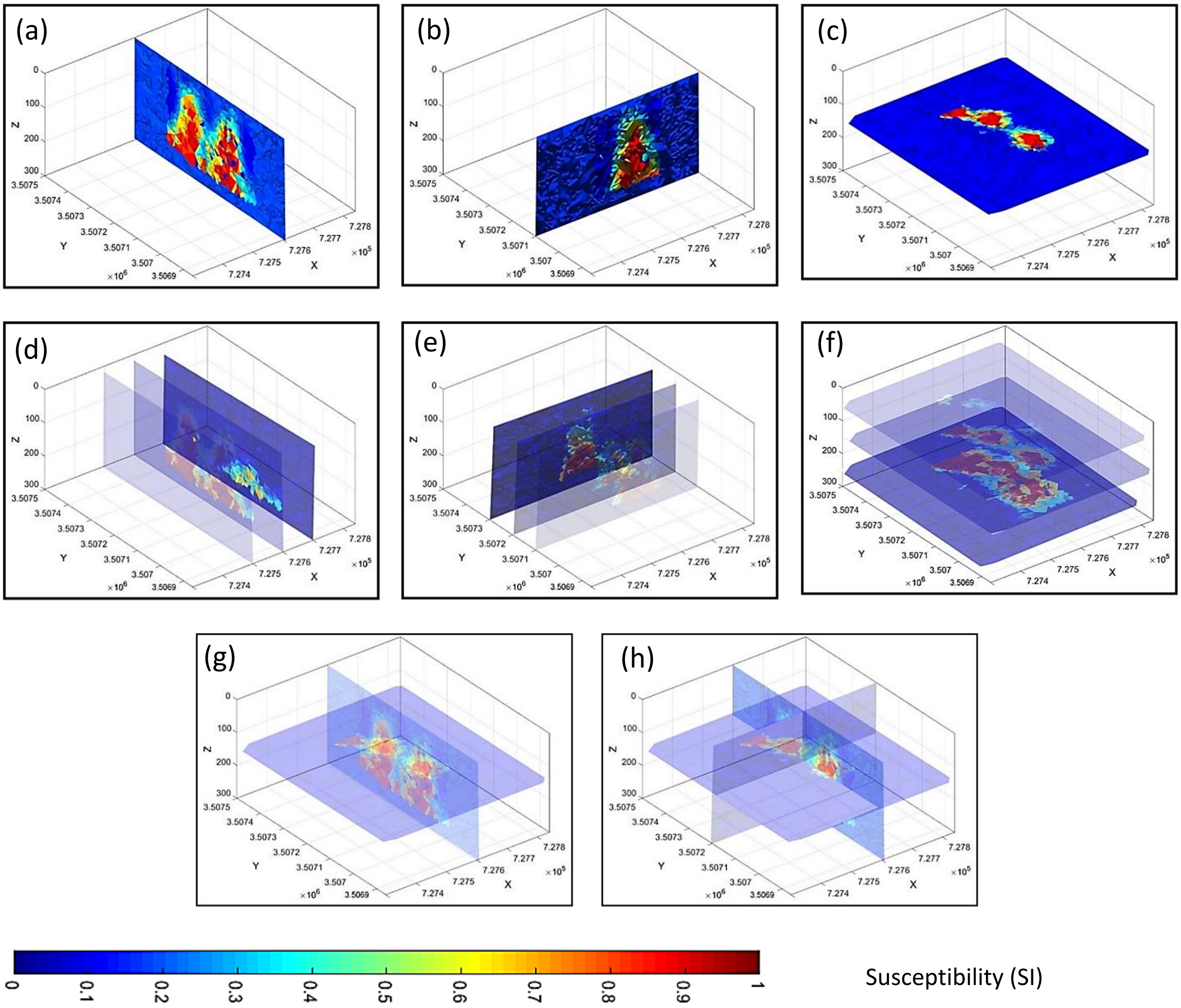

Figure 10. 3D inversion results as cross sections of the magnetic susceptibility at X = 727600 m (a), Y = 3507100 (b), a depth slice at Z = 150 m (c), X = 727500 m, X = 727600 m and X = 727700 m (d), Y = 3507100, Y = 3507200 and Y = 3507300 (e), Z = 50 m, Z = 150 m and Z = 250 m (f), X = 727600 m and Z = 150 (g), and X = 727600 m, Y = 3507200 and Z = 150 m (h),

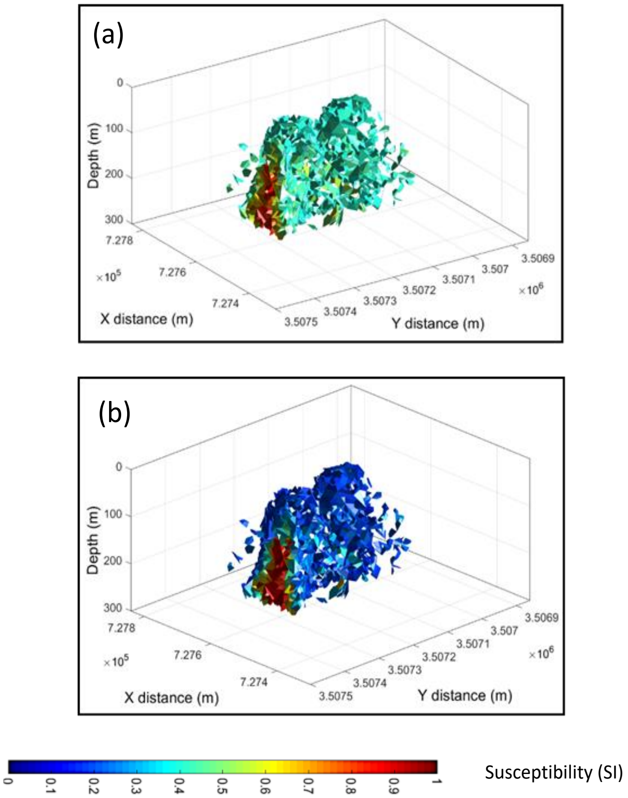

Figure 11. The 3D perspective of magnetic susceptibility with l=100 in inversion process, (a) with cut-off grade of magnetic susceptibility 0.4-0.85 SI, and (b) 0.05-0.9 SI.

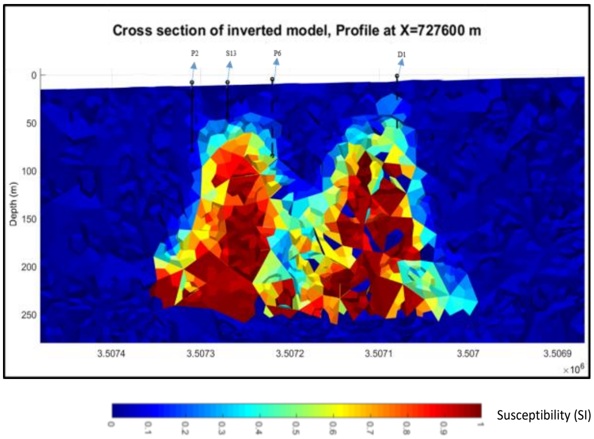

Figure 12. A section of 3D magnetic data inversion with 4 boreholes at X=727600m location with relief topography.

Table3; Enrichment of iron ore mineralization of ore along depth intervals for 4 boreholes

Borehole No.	Total Fe grade (wt%)	Depth interval of Fe ore enrichment(m)
P2	51.94	7.5-13
P6	50.01	34-46
D1	47.85	21.6-23.8
S13	43	9-24

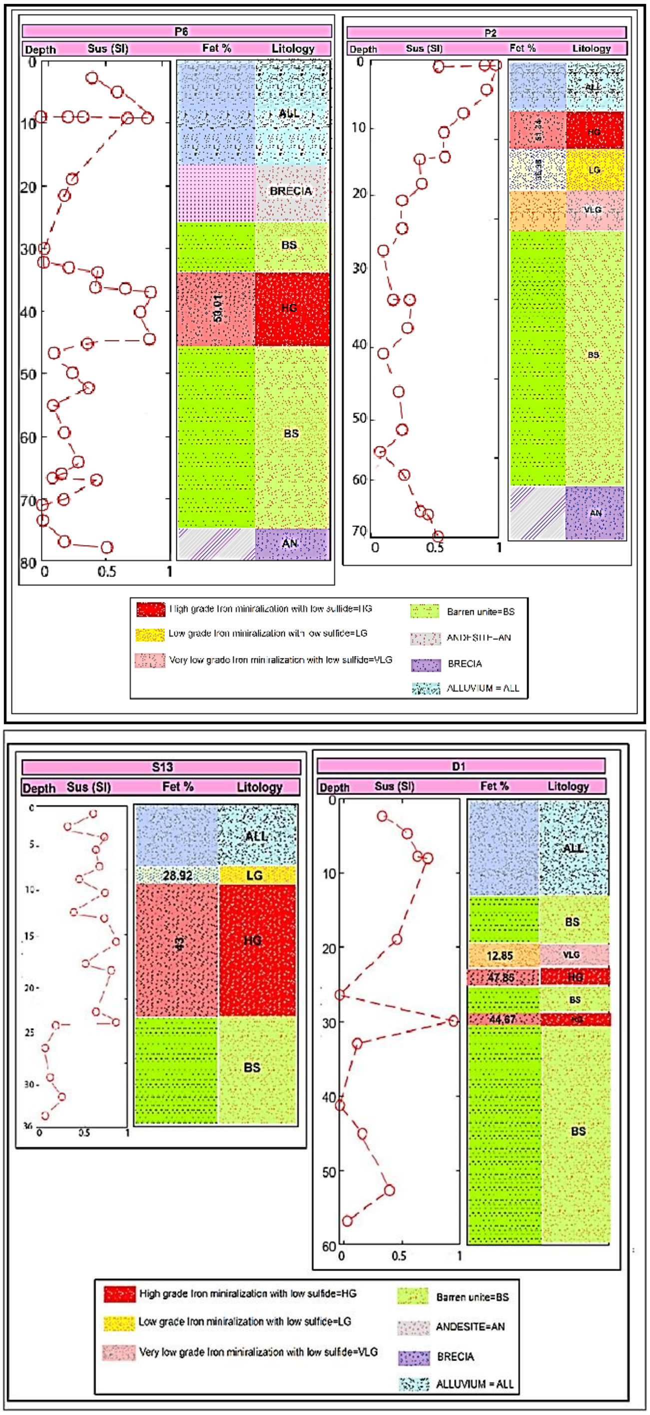

Figure 13. The results of 3D inversion with data provide at locations of 4 drilled boreholes. In order to have a good comparison, on all figures, the order of data, from left to right column, include: the drilling depth (m), inversion results as magnetic susceptibility amounts at any depth, total weight of iron ore grade (as Fet (%)) of drilling, and description of the lithology along depth.

5. Conclusion

Gauss–Legendre quadrature method was used to estimate the magnetic data by unstructured meshing in the subsurface. It was shown that it facilitates preserving accurately the geometry of complex-shaped sources and capturing the impact of rough topography on inverse modeling. To accelerate the inversion the LSQR technique by using a LB solver to replace a kernel by less dimensions is used. The suggested procedure is a kind of fast smooth inversion routine which offers precious views about susceptibility distribution in the subsurface using magnetometry geophysics. The performance of this algorithm was studied for a synthetic complex-shaped body, and then it was employed on a real magnetic data set which provided an accurate outcome. So that the length of mineralization is about 300 meters along the Y axis and its depth has continued up to 250 meters. Also the running time of algorithm execution is around 17.45 seconds. Additionally, the RMS error and the regression coefficient in order were found around 4.9% and 0.90 on real data. At the end the obtained model of iron-bearing mineralization through its magnetic susceptibility model was approved correctly with the consequences of the existing boreholes.

Acknowledgments

We would like to thank the School of Mining Engineering, University of Tehran for supporting this work. We are thankful to the Kim Chaek University of Technology, Pyongyang, and Dr. Gang-Sop Kim for their valuable suggestions and notes on improving this work. Dr. Hossein Jodeiri Akbari Fam is also appreciated for supporting us to work with TetGen package in MATLAB.

REFERENCES

[1] Li, Y., Oldenburg, D.W., 1998. 3-D inversion of gravity data. Geophysics 63, 109–119.

[2] Blakely, R. J. (1996). Potential theory in gravity and magnetic applications. Cambridge university press.

[3] Menke, W., 1989. Geophysical Data Analysis: Discrete Inverse Theory. Academic Press, Inc.

[4] Cella, F., & Fedi, M. (2012). Inversion of potential field data using the structural index as weighting function rate decay. *Geophysical Prospecting*, *60*(2), 313-336.

[5] Abedi, M., Gholami, A., Norouzi, G.H., 2014. 3D inversion of magnetic data seeking sharp boundaries: a case study for a porphyry copper deposit from now Chun in Central Iran. Near Surf. Geophys. 2, 657–666.

[6] Abedi, M., 2019. AIRRLS: an augmented iteratively re-weighted and refined least squares algorithm for inverse modeling of magnetometry data. J. Geol. Res. 3 (1), 16–27.

[7] Essa, K.S., Elhussein, M., 2017. A new approach for the interpretation of magnetic data by a 2-D dipping dike. J. Appl. Geophys. 136, 431–443.

[8] Biswas, A., 2020. Interpretation of gravity anomaly over 2D vertical and horizontal thin sheet with finite length and width. Acta Geophys. 68, 1083–1096.

[9] Zhang, Y., Yan, J., Li, F., Chen, C., Mei, B., Jin, S., Dohm, J.H., 2015. A new bound constraints method for 3D potential field data inversion using Lagrangian multipliers. Geophys. J. Int. 201, 267–275.

[10] Yang, M., Wang, W., Kim Welford, J., Farquharson, C.G., 2019. 3D gravity inversion with optimized mesh based on edge and center anomaly detection. Geophysics 84 (3), G13–G23.

[11] Li, Y., Oldenburg, D.W., 2003. Fast inversion of large-scale magnetic data using wavelet transforms and a logarithmic barrier method. Geophys. J. Int. 152, 251–265.

[12] Leli`evre, P.G., Oldenburg, D.W., Williams, N., 2009. Integrating geological and geophysical data through advanced constrained inversions. Explor. Geophys. 40 (4), 334–341.

[13] Fournier, D., Oldenburg, D.W., 2019. Inversion using spatially variable mixed ℓp norms. Geophys. J. Int. 218 (1), 268–282.

[14] Portniaguine, O., Zhdanov, M.S., 2002. 3D magnetic inversion with data compression and image focusing. Geophysics 67, 1532–1541.

[15] Jahandari, H., & Farquharson, C. G. (2015). Finite-volume modelling of geophysical electromagnetic data on unstructured grids using potentials. Geophysical Journal International, 202(3), 1859-1876.

[16] Jahandari, H., Ansari, S.M., Farquharson, C.G., 2017. Comparison between staggered grid finite–volume and edge–based finite–element modelling of geophysical electromagnetic data on unstructured grids. J. Appl. Geophys. 138, 185–197.

[17] Liu, S., Hu, X., Xi, Y., Liu, T., 2015a. 2D inverse modeling for potential fields on rugged observation surface using constrained Delaunay triangulation. Comput. Geosci. 76, 18–30.

[18] Singh, A., 2020. Triangular grid-based fuzzy cross-update inversion of gravity data: case studies from mineral exploration. Nat. Resour. Res. 29, 459–471.

[19] Baranwal, V.C., Franke, A., Borner, R.U., Spitzer, K., 2011. Unstructured grid based 2-D inversion of VLF data for models including topography. J. Appl. Geophys. 75, 363–372.

[20] Darijani, M., Farquharson, C.G., Leli`evre, P.G., 2020. Clustering and constrained inversion of seismic refraction and gravity data for overburden stripping: application to uranium exploration in the Athabasca Basin, Canada. Geophysics 85 (4), B133–B146.

[21] Cai, Y., & Wang, C. Y. (2005). Fast finite-element calculation of gravity anomaly in complex geological regions. Geophysical Journal International, 162(3), 696-708.

[22] Key, K., & Ovall, J. (2011). A parallel goal-oriented adaptive finite element method for 2.5-D electromagnetic modelling. Geophysical Journal International, 186(1), 137-154.

[23] Jahandari, H., & Farquharson, C. G. (2013). Forward modeling of gravity data using finite-volume and finite-element methods on unstructured grids. Geophysics, 78(3), G69-G80.

[24] Kim, G. S., Ryu, J. C., Sin, O. C., Han, J. S., & Kim, S. G. (2014). Body-growth inversion of magnetic data with the use of non-rectangular grid. Journal of Applied Geophysics, 102, 47-61.

[25] Gross, L., Altinay, C., & Shaw, S. (2015). Inversion of potential field data using the finite element method on parallel computers. Computers & geosciences, 84, 61-71.

[26] Roussel, C., Verdun, J., Cali, J., & Masson, F. (2015). Complete gravity field of an ellipsoidal prism by Gauss–Legendre quadrature. Geophysical Supplements to the Monthly Notices of the Royal Astronomical Society, 203(3), 2220-2236.

[27] Schaa, R., Gross, L., & Du Plessis, J. (2016). PDE-based geophysical modelling using finite elements: examples from 3D resistivity and 2D magnetotellurics. Journal of Geophysics and Engineering, 13(2), S59-S73.

[28] Li, J., Lu, X., Farquharson, C. G., & Hu, X. (2018). A finite-element time-domain forward solver for electromagnetic methods with complex-shaped loop sources. Geophysics, 83(3), E117-E132.

[29] Uwiduhaye, J. D. A., Mizunaga, H., & Saibi, H. (2019). A case history: 3-D gravity modeling using hexahedral element in Kinigi geothermal field, Rwanda. Arabian Journal of Geosciences, 12(3), 86.

[30] Codd, A. L., Gross, L., & Aitken, A. (2021). Fast multi-resolution 3D inversion of potential fields with application to high-resolution gravity and magnetic anomaly data from the Eastern Goldfields in Western Australia. Computers & Geosciences, 157,

104941.

[31] Toushmalani, R., & Saibi, H. (2015). Fast 3D inversion of gravity data using Lanczos bidiagonalization method. Arabian Journal of Geosciences, 8(7), 4969-4981.

[32] Rezaie, M., Moradzadeh, A., & Kalateh, A. N. (2017). Fast 3D inversion of gravity data using solution space priorconditioned lanczos bidiagonalization. Journal of Applied Geophysics, 136, 42-50.

[33] Tikhonov, A. N., & Arsenin, V. I. (1977). Solutions of ill-posed problems (Vol. 14).

[34] Martin, R., Monteiller, V., Komatitsch, D., Perrouty, S., Jessell, M., Bonvalot, S., & Lindsay, M. (2013). Gravity inversion using wavelet-based compression on parallel hybrid CPU/GPU systems: application to southwest Ghana. Geophysical Journal International, 195(3), 1594-1619.

[35] Kim, Kang-sop, Hu, Xiang-yun, et al., 2009. Study on isoparametric finite-element integral algorithm of gravity and magnetic anomaly for body with complex shape. Oil Geophys. Prospect. 44 (2), 231–239 (in Chinese).

[36] Pilkington, M. (1997). 3-D magnetic imaging using conjugate gradients. Geophysics, 62(4), 1132-1142.

[37] Meng, Z., Li, F., Xu, X., Huang, D., & Zhang, D. (2017). Fast inversion of gravity data using the symmetric successive over-relaxation (SSOR) preconditioned conjugate gradient algorithm. Exploration Geophysics, 48(3), 294-304.

[38] Moradzadeh, A. (1998). Electrical imaging of the Adelaide geosyncline using magnetotellurics (MT) (Doctoral dissertation, Flinders University of South Australia).

[39] Zhdanov, M. S. (2002). Geophysical inverse theory and regularization problems (Vol. 36). Elsevier.

[40] Abedi, M. (2022). Cooperative fuzzy-guided focused inversion for unstructured mesh modeling of potential feld geophysics, a case study for imaging an oil-trapping structure. Acta Geophysica, doi.org/10.1007/s11600-022-00857-w.

[41] Danaei, K., Moradzadeh, A., Norouzi, G. H., Smith, R., Abedi, M., & Fam, H. J. A. (2022). 3D inversion of gravity data with unstructured mesh and least-squares QR-factorization (LSQR). Journal of Applied Geophysics, 206, 104781.

[42] Abedi, M., Gholami, A., Norouzi, G. H., & Fathianpour, N. (2013). Fast inversion of magnetic data using Lanczos bidiagonalization method. Journal of Applied Geophysics, 90, 126-137.

[43] Daliran, F., Stosch, H.G., Williams, P., 2010. Lower Cambrian iron oxide-apatite-REE (U) deposits of the Bafq district, east-Central Iran. In: Corriveau, L., Mumin, A.H. (Eds.), Exploring for Iron Oxide Copper-Gold Deposits. Canada and Global Analogues. Geological Society of Canada Short Course Notes 20, St. John's, Newfoundland Canada, pp. 147–159.

[44] Nabatian, Gh., Rastad, E., Neubauer, F., Honarmand, M., Ghaderi, M., 2015. Iron and FeMn mineralisation in Iran: implications for Tethyan metallogeny. Aust. J. Earth Sci. 62, 211–241.

[45] Alamdar, K., 2016a. Interpretation of the magnetic data from Shavaz iron ore using enhanced local wavenumber (ELW) and comparison with Euler deconvolution method. Arab. J. Geosci. 9, 597.

[46] Alamdar, K., 2016b. Development of the gradient ratio method for depth estimation of the subsurface bodies using Bouguer gravity map data. J. Res. Appl. Geophys. 1 (2), 131–141.

[47] Rahimi, E. (2018), Depth estimation of the potential field data using wavelet transform, (case study: gravity and magnetic data from Shavaz iron ore mine in Yazd). M.Sc. thesis (in Persian), Department of Mining & Metallurgical Engineering, Yazd University, Iran.

[48] Abedi, M. (2020). A focused and constrained 2D inversion of potential field geophysical data through Delaunay triangulation, a case study for iron-bearing targeting at the Shavaz deposit in Iran. Physics of the Earth and Planetary Interiors 309, 106604.